Volume 5 | Number 11 | 21 March 2017 | Pages 2735–2960

Journal of Materials Chemistry C

Materials for optical, magnetic and electronic devices

rsc.li/materials-c

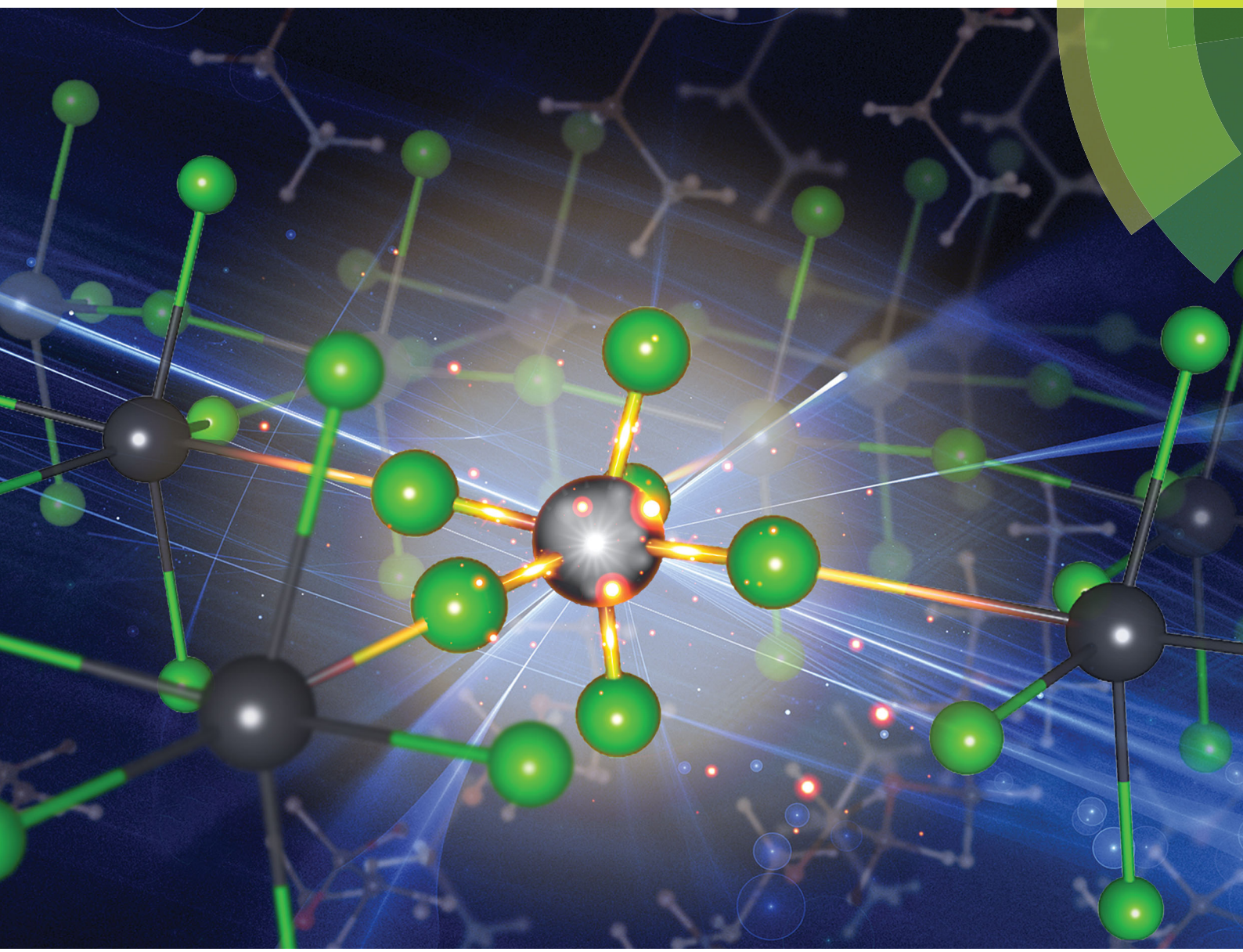

ISSN 2050-7526

ROYAL SOCIETY OF CHEMISTRY

COMMUNICATION

Cesare Soci *et al.*

Polaron self-localization in white-light emitting hybrid perovskites

Journal of Materials Chemistry C

COMMUNICATION

View Article Online
View Journal | View Issue

Cite this: J. Mater. Chem. C, 2017, 5, 2771

Received 21st January 2017,
Accepted 3rd February 2017

DOI: 10.1039/c7tc00366h

rsc.li/materials-c

Polaron self-localization in white-light emitting hybrid perovskites†

Daniele Cortecchia,[ab] Jun Yin,[cd] Annalisa Bruno,[b] Shu-Zee Alencious Lo,[c] Gagik G. Gurzadyan,‡[c] Subodh Mhaisalkar,[b] Jean-Luc Brédas[d] and Cesare Soci*[ce]

Two-dimensional (2D) perovskites with the general formula $APbX_4$ are attracting increasing interest as solution processable, white-light emissive materials. Recent studies have shown that their broadband emission is related to the formation of intra-gap colour centres. Here, we provide an in-depth description of the charge localization sites underlying the generation of such radiative centres and their corresponding decay dynamics, highlighting the formation of small polarons trapped within their lattice distortion field. Using a combination of spectroscopic techniques and first-principles calculations to study the white-light emitting 2D perovskites (EDBE)$PbCl_4$ and (EDBE)$PbBr_4$, we infer the formation of Pb_2^{3+}, Pb^{3+}, and X_2^- (where X = Cl or Br) species confined within the inorganic perovskite framework. Due to strong Coulombic interactions, these species retain their original excitonic character and form self-trapped polaron–excitons acting as radiative colour centres. These findings are expected to be relevant for a broad class of white-light emitting perovskites with large polaron relaxation energy.

Introduction

After demonstrating outstanding performance in photovoltaic[1] and photodetector[2] devices, solution processable hybrid perovskites are currently in the spotlight for light-emitting applications,[3] such as light-emitting diodes (LEDs),[4,5] light-emitting transistors (LETs)[6] and tunable lasers.[7,8] Recent research suggests that two-dimensional (2D) perovskites[9]—in which the intrinsic layered configuration is responsible for strong exciton confinement within the inorganic interlayers—[10–12] have superior light-emitting properties compared to conventional three-dimensional perovskites, such as methylammonium lead iodide $MAPbI_3$.[13,14] Broadband, white-light generation has been reported in various 2D perovskites with the general formula $APbX_4$ (X = Cl, Br and A = bidentate organic cation), which makes them particularly attractive for solid-state lighting and displays.[15] In earlier works on closely related layered materials with the formula $Cd_{2-x}Zn_xE_2$(alkylamine) (E = S, Se, and Te),[16–18] the broadband luminescence was ascribed to deep surface states related to the large effective surface area intrinsic to the layered structure.[17,19] In the 2D perovskite (API)$PbBr_4$ (API = *N*-(3-aminopropyl)imidazole), the broadband photoluminescence spectrum was attributed by Li *et al.* to emission from the organic linker, upon energy transfer from the inorganic framework.[20] On the other hand, Dohner *et al.* related the highly efficient broadband emission of the perovskites (*N*-MEDA)$[PbBr_{4-x}Cl_x]$ (*N*-MEDA = *N*1-methylethane-1,2-diammonium)[21] and (EDBE)PbX_4 (EDBE = 2,2-(ethylenedioxy)-bis(ethylammonium), X = Cl, Br)[22] either to distributed trap states or to the formation of self-trapped excitons. The hypothesis of exciton self-trapping was also supported by Yangui *et al.* who reported similar emission in $(C_6H_{11}NH_3)_2PbBr_4$,[23] and more recently by Hu *et al.* who probed photocarrier dynamics by THz spectroscopy.[24] These latest works have highlighted the importance of self-trapping in photoluminescence broadening; however, a comprehensive description of the charge localization sites in relation to the hosting perovskite structure is still lacking. In this work, we study the white-light emitting 2D perovskites (EDBE)PbX_4 (X = Cl, Br) characterized by different orientations of the inorganic sheets, and provide further evidence for the photogeneration of polaronic species deriving from self-trapping of charge carriers at specific inorganic lattice sites. Details of the band structure and electronic transitions of these compounds are obtained by a combination of absorption and

[a] Interdisciplinary Graduate School, Nanyang Technological University, Singapore 639798, Singapore
[b] Energy Research Institute @ NTU (ERI@N), Research Techno Plaza, Nanyang Technological University, 50 Nanyang Drive, Singapore 637553, Singapore
[c] Division of Physics and Applied Physics, School of Physical and Mathematical Sciences, Nanyang Technological University, 21 Nanyang Link, Singapore 637371, Singapore. E-mail: csoci@ntu.edu.sg
[d] Laboratory for Computational and Theoretical Chemistry and Advanced Materials, Division of Physical Science and Engineering, King Abdullah University of Science and Technology, Thuwal 23955-6900, Saudi Arabia
[e] Centre for Disruptive Photonic Technologies, TPI, Nanyang Technological University, 21 Nanyang Link, Singapore 637371, Singapore

† Electronic supplementary information (ESI) available: X-ray diffraction pattern (XRD), Raman spectra, optical data (exciton binding energy extraction, fitting details), excitation dependent ultrafast dynamics, transient absorption (TA) measurements, and charge density maps. See DOI: 10.1039/c7tc00366h

‡ Current address: Institute of Artificial Photosynthesis, State Key Laboratory of Fine Chemicals F-209, Dalian University of Technology, Dalian, 116024, China.

luminescence spectroscopies at various temperatures and first-principles density functional theory (DFT) calculations, which indicate that the optical properties are strongly correlated to charge–charge and charge–phonon interactions induced by the layered structure. Consequently, photoluminescence is generated efficiently upon excitation of the low energy excitonic absorption, whilst fast non-radiative thermalization dominates at higher energy excitation. Three main groups of emitters are found to contribute to the broad luminescence spectrum with large Stokes shifts; based on the charge density maps obtained from DFT, these are identified as Pb_2^{3+}, Pb^{3+}, and X_2^- (where X = Cl or Br) small-polaron species confined within the inorganic perovskite framework.

Results and discussion

The white light emitting hybrid perovskites (EDBE)$PbCl_4$ and (EDBE)$PbBr_4$ used in this study were synthetized by spin-coating to obtain high-quality and ultra-smooth thin films (see Fig. S1, ESI†). In agreement with previous results,[22] (EDBE)$PbCl_4$ crystallizes as a ⟨100⟩-oriented perovskite,[10] forming a 2D structure of alternating flat inorganic layers and organic sheets of the di-ammonium cation $EDBE^{2+}$ (Fig. 1a, inset). Conversely, (EDBE)$PbBr_4$ has the typical structure of a ⟨110⟩-oriented 2D perovskite,[10] characterized by rippled organic and inorganic sheets and distorted geometry (Fig. 1b, inset). The absorption spectra of both materials (Fig. 1a and b) can be qualitatively divided into two main regions: a high-energy absorption continuum with an onset around 4 eV and 3.75 eV for the chlorine and bromine substituted compounds, and the sharp E-bands peaked at 3.72 eV and 3.32 eV, respectively. The E-bands are due to the excitonic absorption typical of layered perovskites; similar to quantum well structures, excitonic absorption is enhanced here by quantum confinement effects due to the difference in the optical gap and polarizability between the organic barriers and the inorganic wells.[25] The resulting image charge effect[11,25] substantially increases the Coulomb interaction between electrons and holes within the wells, accounting for the large exciton binding energies (412 meV and 365 meV for (EDBE)$PbCl_4$ and (EDBE)$PbBr_4$, respectively) deduced from the low-temperature absorption spectra of the two compounds (see details provided in Fig. S2, ESI†). At low temperature, the excitonic band of (EDBE)$PbCl_4$ splits into a vibronic progression (Fig. 1c), consistent with the Franck Condon replicas of the 16, 24, 49 and 68 meV phonons measured in the Raman spectra (Fig. S3, ESI†).[26] Quantitative fitting of the excitonic replicas (red line in Fig. 1c) reveals the coupling strength of specific phonon modes through the amplitude of the Huang–Rhys factors (blue bars in Fig. 1c; see also Table S1 and description of the fitting procedure in the ESI†). While the strong vibrational modes of the 16 and

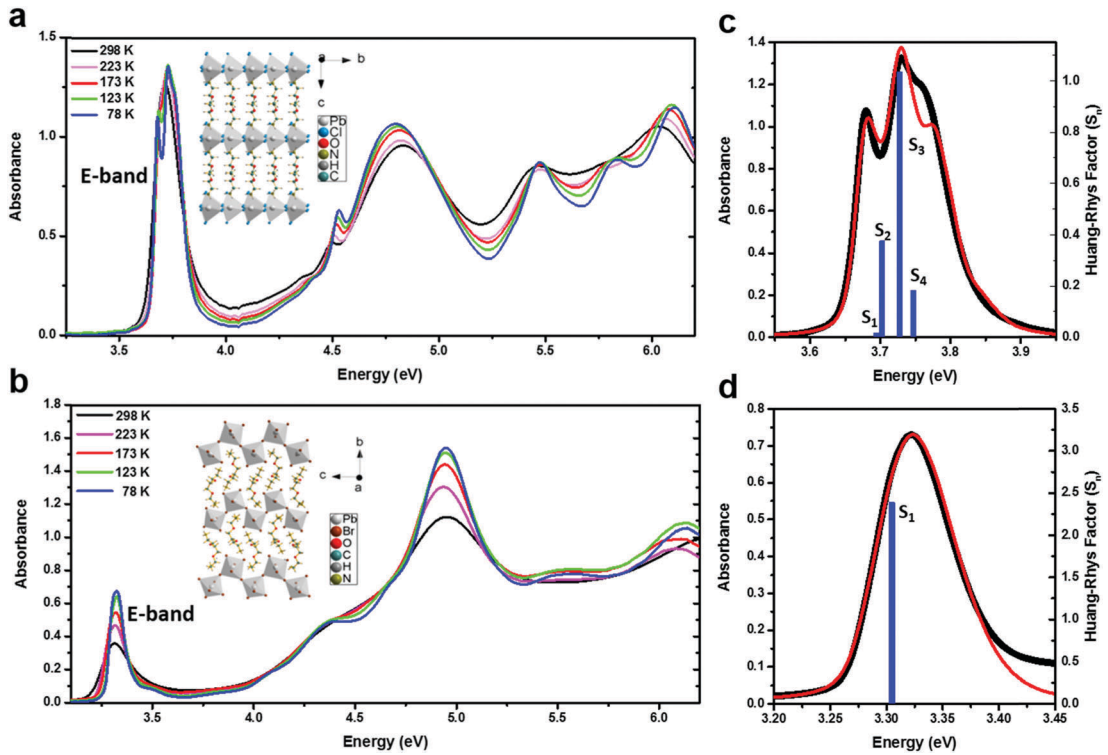

Fig. 1 Temperature dependent absorption spectra. Steady state absorption of (a) (EDBE)$PbCl_4$ and (b) (EDBE)$PbBr_4$. Chlorine replacement with bromine causes 400 meV redshift of the E-band, while it has minor effects on the high-energy part of the spectra. Insets show the layered structure of the ⟨100⟩-oriented perovskite (EDBE)$PbCl_4$ (a, inset) and the ⟨110⟩-oriented (EDBE)$PbBr_4$ (b, inset). Fitting of the excitonic absorption at 78 K using a Frank–Condon vibronic progression (see equation in ESI†). (EDBE)$PbCl_4$ (c) shows a complex vibronic structure due to the coupling with four phonons (16, 24, 49, and 68 meV), while (EDBE)$PbBr_4$ (d) shows a single band consistent with coupling to a single 19 meV phonon (black line: experimental absorption; red line: fitting).

24 meV phonons, due to the stretching vibrations of the Pb–X bonds in the inorganic scaffold,[27] are consistent with exciton localization within the inorganic quantum wells, we find an unexpectedly strong coupling with the 49 and 64 meV high energy phonons characteristic of the EDBE vibrations (Fig. S3, ESI†). This may be due to the interaction between inorganic and organic layers, which are strongly linked to the lead halide framework through charge-assisted hydrogen bonds. While the band splitting is evident in the planar ⟨100⟩ structure of (EDBE)$PbCl_4$, the vibronic features of the corrugated ⟨110⟩-oriented (EDBE)$PbBr_4$ cannot be resolved even at 78 K (Fig. 1d). This suggests that excitons in (EDBE)$PbBr_4$ couple only to the low-energy phonons of the Pb–X framework, consistent with the Franck Condon fitting of the main excitonic absorption peak with a single 19 meV phonon, which corresponds to the highest vibrational mode of the $PbBr_4^{2-}$ inorganic lattice (150 cm^{-1} Raman mode in Fig. S3, ESI†).

Calculations of the band structure and density of states at the density functional theory (DFT) level provide additional details on the higher-energy inter-band transitions. The unit cells of the optimized crystal structure of the two perovskites, the starting point for the band structure calculations, are shown in Fig. 2a and b. When using the general gradient approximation (GGA)/Perdew–Burke–Ernzerhof (PBE) functional without spin–orbit coupling (SOC), (EDBE)$PbCl_4$ is calculated to have a direct bandgap (3.32 eV) at the Γ point, and (EDBE)$PbBr_4$ shows a direct bandgap (2.55 eV) at the A point of the respective Brillouin zones (Fig. 2c and d). Including SOC effects in the calculations retains the same band curvatures but with a change in conduction band degeneracies and reduced bandgaps of 2.49 eV for (EDBE)$PbCl_4$ and 2.00 eV for (EDBE)$PbBr_4$. The projected density of states (PDOS) reveals that in both materials the valence band consists of p orbitals of the halogen (Cl-3p, Br-4p) and Pb-6s orbitals, while the conduction band is mainly composed of Pb-6p orbitals. This indicates that the high-energy absorption continuum is due to the inter-band electronic transitions of the kind $Pb^{2+}(6s)Cl^{-}(3p) \rightarrow Pb^{2+}(6p)$ and $Pb^{2+}(6s)Br^{-}(4p) \rightarrow Pb^{2+}(6p)$ (similar to the situation in the parent lead halide PbX_2 compounds[28]), and confirms that the E-bands are due to excitons confined within the closely spaced inorganic layers. The organic EDBE layers contribute little to the top region of the valence band and the bottom region of the conduction band; this is similar to three-dimensional Pb-based hybrid perovskites, such as $CH_3NH_3PbI_3$.[29] However, even though the EDBE organic cations do not actively contribute to the inter-band transitions, which are primarily due to the

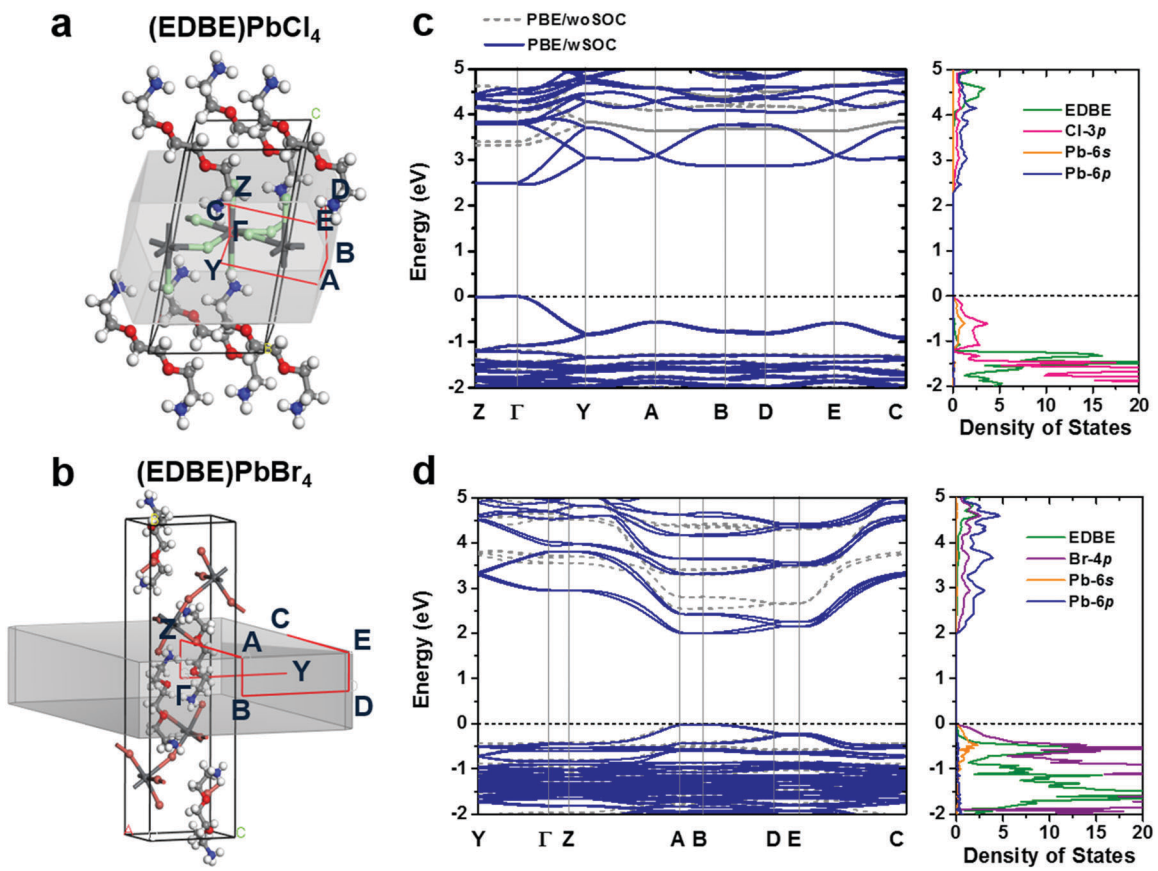

Fig. 2 Density functional theory (DFT) calculations at the GGA/PBE level. Optimized crystal structure, obtained using the experimental cell parameters as a starting point, for (a) (EDBE)$PbCl_4$ and (b) (EDBE)$PbBr_4$. Band structures (with and without inclusion of spin–orbital coupling – wSOC and woSOC) and projected density of states with SOC of (c) (EDBE)$PbCl_4$ and (d) (EDBE)$PbBr_4$. Even in the absence of SOC, the resulting bandgap values are lower than the experimental absorption edges, namely 3.32 eV for (EDBE)$PbCl_4$ and 2.55 eV for (EDBE)$PbBr_4$ (see Fig. S2, ESI†). PBE/wSOC lowers the bandgap energies to 2.49 and 2.00 eV for (EDBE)$PbCl_4$ and (EDBE)$PbBr_4$, respectively.

inorganic scaffold, they are responsible for the emergence of the sharp E-band absorption, through the formation of highly confined excitonic states within the layered inorganic quantum wells of the 2D perovskite structure.

Upon photoexcitation, (EDBE)$PbCl_4$ and (EDBE)$PbBr_4$ emit extremely broadband luminescence throughout the entire visible range, with unusually large "Stokes shifts" of the emission peak relative to the maximum of the E-band (1.38 eV and 1.00 eV, respectively, see Fig. 3). This is in sharp contrast with the narrow emission spectra and small Stokes shift typical of 2D excitonic perovskites like phenethylammonium and butylammonium based perovskites.[30,31] Despite the broad absorption spectra shown in Fig. 1, efficient fluorescence is observed exclusively within a narrow band of excitation energies corresponding to the E-bands. In particular, the photoexcitation maps of (EDBE)$PbCl_4$ (Fig. 3a and b) reveal two maxima peaking at excitation energies of 3.84 eV and 3.74 eV at low temperature, which trace the spectral shape of vibronic replicas in the excitonic absorption band (Fig. 1a). The slightly wider spacing of the two peaks in the excitation spectrum can be expected to arise from differences between the vibrational modes of the excited state compared to the ground state. Similarly, the photoexcitation map of (EDBE)$PbBr_4$ shows a single maximum at E_{exc} = 3.32 eV (Fig. 3c and d), which matches perfectly the excitonic absorption line shape (Fig. 1b). Unexpectedly, excitation at higher photon energies into the band continuum yields weaker and progressively narrower emission spectra. This is also reflected in time-resolved photoluminescence (TRPL) measurements, where efficient radiative recombination with a characteristic decay time of $\tau \approx 3$ ns is achieved upon resonant excitation of the excitonic absorption, while excitation of higher energy transitions (*e.g.*, E_{exc} = 4.66 eV) results in extremely fast photoluminescence decay ($\tau \ll 40$ ps), likely due to deactivation through nonradiative decay channels (Fig. S4 and Table S2, ESI†). This indicates that the formation of radiative states is conditional to the creation of excitons, like conventional traps, which would be populated upon thermalization from high-energy states, regardless of the photoexcitation energy.

Notwithstanding the strong dependence of the energy of the E-band on material composition, the emission profiles of the two compounds are surprisingly similar (Fig. 4a and c and Fig. S5, ESI†). At room temperature, both emission spectra peak at 2.34 eV, with a full width at half maximum (FWHM) of 650 meV. This observation strongly suggests that the broadband radiative emission involves analogous intermediate states. To determine the emissive states, the luminescence spectra of (EDBE)$PbCl_4$ and (EDBE)$PbBr_4$ were analysed by principal component fitting (Fig. S6 and S7, ESI†). At each temperature, three main components contributing to white-light emission can be identified, hereafter denoted *W*1, *W*2, and *W*3 (the central energy of

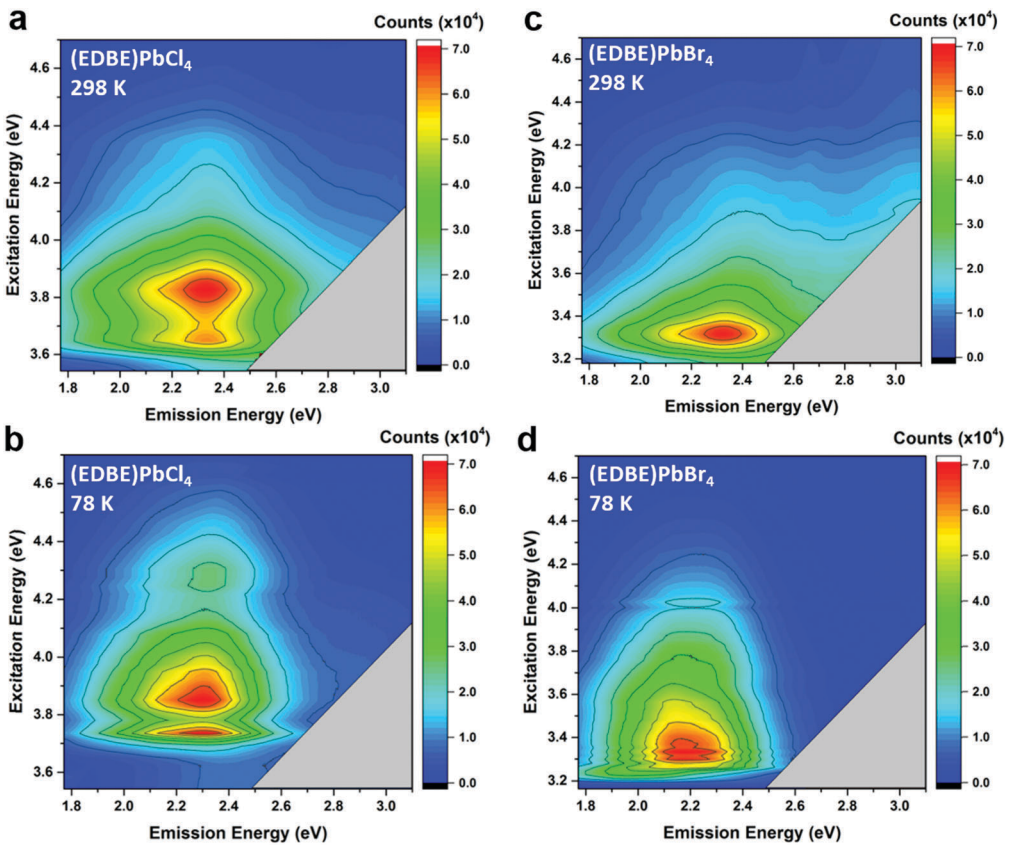

Fig. 3 Luminescence photoexcitation maps. Contour plots of the photoluminescence emission intensity as a function of emission and excitation energies for (EDBE)$PbCl_4$ (left panels a and b) and (EDBE)$PbBr_4$ (right panels c and d). Maps in the top panels (a and c) were recorded at room temperature (T = 298 K) while those in the bottom panels (b and d) were recorded at low temperature (T = 78 K).

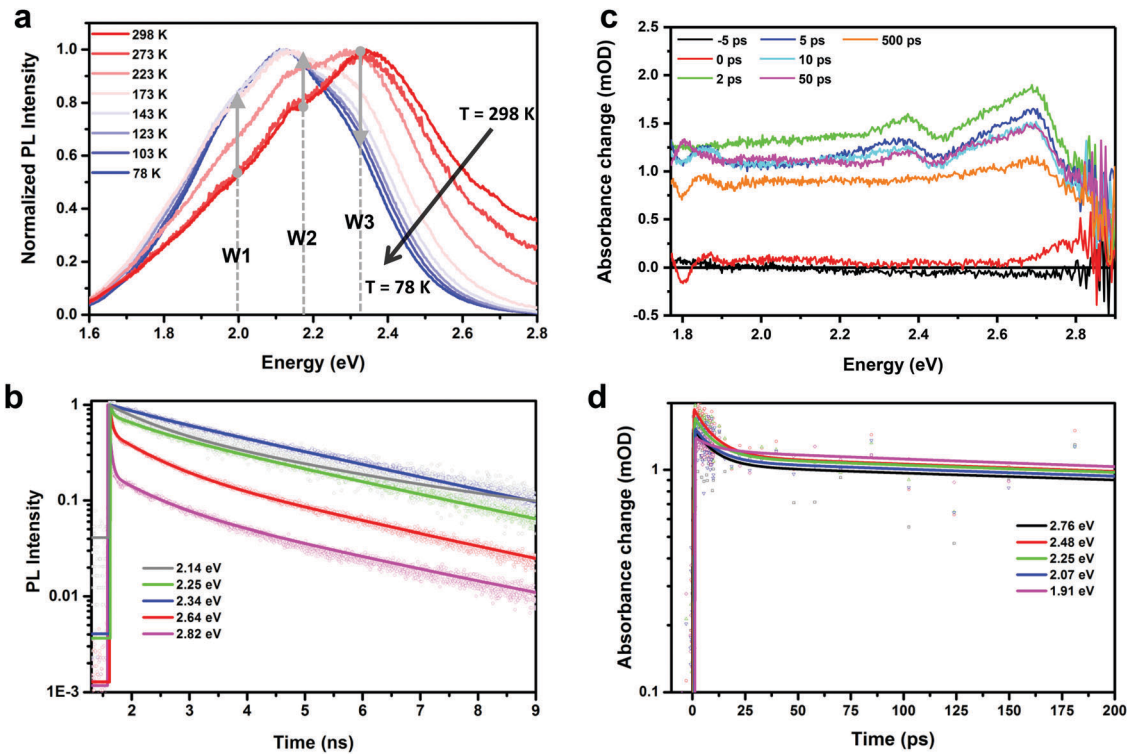

Fig. 4 Multicomponent analysis of broadband photoluminescence and transient absorption (TA) measurements of (EDBE)$PbBr_4$. (a) Temperature-dependent steady state photoluminescence spectrum. The dashed lines indicate the temperature-independent energy of the three principal components ($W1$ = 1.98 eV, $W2$ = 2.14 eV and $W3$ = 2.32 eV) determined from the analysis of all photoluminescence spectra (Fig. S7, ESI†). (b) Spectral dependence of time resolved photoluminescence (TRPL) performed under excitation energy E_{exc} = 3.26 eV. (c) Transient absorption (TA) spectra under resonant excitation of the excitonic peak (E_{exc} = 3.26 eV) and (d) corresponding decay dynamics at different probing energies.

these components in (EDBE)$PbBr_4$ is indicated by dashed lines in Fig. 4a). The large and irregular energy spacing between $W1$, $W2$, and $W3$ (~160–190 meV) rules out their possible vibronic nature, as seen earlier in the case of E-band absorption (Fig. 1b and d). As expected for deep levels, the spectral positions of $W1$, $W2$ and $W3$ are nearly independent of temperature (Fig. S6 and S7, ESI;† note that the change in relative weight of each component is responsible for the apparent red-shift of the total emission at lower temperatures). On the other hand, the total photoluminescence intensity increases significantly at low temperature due to the reduction of line broadening and non-radiative recombination. Fitting of the Arrhenius plots[32] of the integrated photoluminescence intensity yields thermal activation energies of E_a = 147 meV and E_a = 105 meV for (EDBE)$PbCl_4$ and (EDBE)$PbBr_4$, respectively (Fig. S5, ESI†). Such large activation energies imply the existence of deep radiative states, with energy much larger than thermal vibrations.

The existence of multiple radiative components was further confirmed by the spectral dependence of photoluminescence decay dynamics. The transient photoluminescence decay of (EDBE)$PbBr_4$ (Fig. 4b) was found to contain at least three components, with characteristic decay times of τ_1 = 40 ps, τ_2 = 0.74 ns, and τ_3 = 3.24 ns, as determined by global fitting of the entire dataset in Fig. 4b with multiple exponential waveforms (Table 1). We ascribe the ultrafast decay, with larger weight at high emission energies (2.82 eV and 2.64 eV), to hot exciton emission, which would have marginal contribution to steady-state luminescence. On the other hand, the slower components prevailing at low emission energies can be related to the $W1$–$W3$ emitters. Since the spectral dependence of amplitude A3 closely resembles that of the $W3$ emission profile (Table 1 and Fig. S7, ESI†), we assign τ_3 to this particular emitter, while τ_2 could result from the superposition of comparable characteristic lifetimes of $W1$ and $W2$, which cannot be fully resolved by the fitting.

Transient absorption (TA) measurements performed with excitation resonant to the E-bands show the formation of an unstructured excited-state absorption spanning the entire visible spectral range (Fig. 4c and Fig. S8, ESI†), consistent with the formation of colour centres distributed throughout the bandgap.

Table 1 Time resolved photoluminescence (TRPL) parameters for (EDBE)$PbBr_4$. The characteristic lifetimes (τ) and amplitudes (A) were extracted from the global fitting of the five decays with a three-exponential decay function (E_{exc} = 3.26 eV). Fit result for τ_1 = 40 ps indicates that in fact $\tau_1 \ll$ 40 ps, since τ_1 is very close to the time resolution of our setup (IRF = 20–30 ps)

Emission energy (eV)	τ_1 (ns)	A_1	τ_2 (ns)	A_2	τ_3 (ns)	A_3
2.82	0.04	0.81	0.74	0.10	3.24	0.10
2.64	0.04	0.49	0.74	0.28	3.24	0.23
2.34	0.04	0.00	0.74	0.09	3.24	0.91
2.25	0.04	0.20	0.74	0.18	3.24	0.63
2.14	0.04	0.00	0.74	0.41	3.24	0.59

The absence of stimulated emission further confirms that the broadband photoluminescence is not directly correlated to singlet excited states. The formation time of the trapped states, as determined from the rise of the photoinduced absorption, is comparable to our instrumental resolution (~100 fs). This is in agreement with the ultrafast self-trapping of charge carriers reported by Hu *et al.*,[24] which was attributed to the coupling to vibrational modes of the inorganic scaffold. The TA decay dynamics contain two components, and are nearly independent of probe photon energy (Fig. 4d and Table S3, ESI†). In the case of (EDBE)$PbBr_4$, the fast component ($\tau_1 \approx 10$ ps) can be related to the excitonic emission ($\tau \ll 40$ ps) observed in TRPL with non-resonant excitation. We tentatively ascribe it to the population of the first excited singlet state (S_1) undergoing absorption to higher singlet states (S_N). Conversely, the slower process with decay time $\tau_2 = 0.74$ ns matches well the τ_2 decay time measured in TRPL, and may be indicative of the excited-state absorption from the intra-gap trap states.

The nature of the emissive states is further elucidated by our first-principles DFT-PBE calculations of the charge density distributions. In a way similar to organic semiconductors,[33,34] polaronic effects have been recently considered in order to understand the charge transport and light emission characteristics of hybrid and inorganic perovskites.[24,35–43] Notably, it was proposed that the formation of small polarons stabilized by collective rotations of methylammonium cations[41] may play a role in the photodegradation of $MAPbI_3$.[40] In crystals where photoexcitation causes significant lattice deformation, holes and electrons may be localized at specific lattice sites by their own distortion field, giving rise to self-trapped electrons (STEL) and self-trapped holes (STH).[44,45] This process can also bring temporary short-range chemical bonding between nearest neighbour ions (molecular polaron).[46] When self-localized carriers are bound electron–hole pairs, the resulting species are described as polaron–excitons, PE. Self-trapping phenomena have been extensively studied and frequently observed in alkali, alkaline-earth, and perovskite-structure halides (*e.g.*, KCl, CaF_2, $KMgF_3$).[45,47] Similarly, charge self-trapping at low temperature in lead halides PbX_2 (X = Cl, Br) is known to yield large Stokes shift

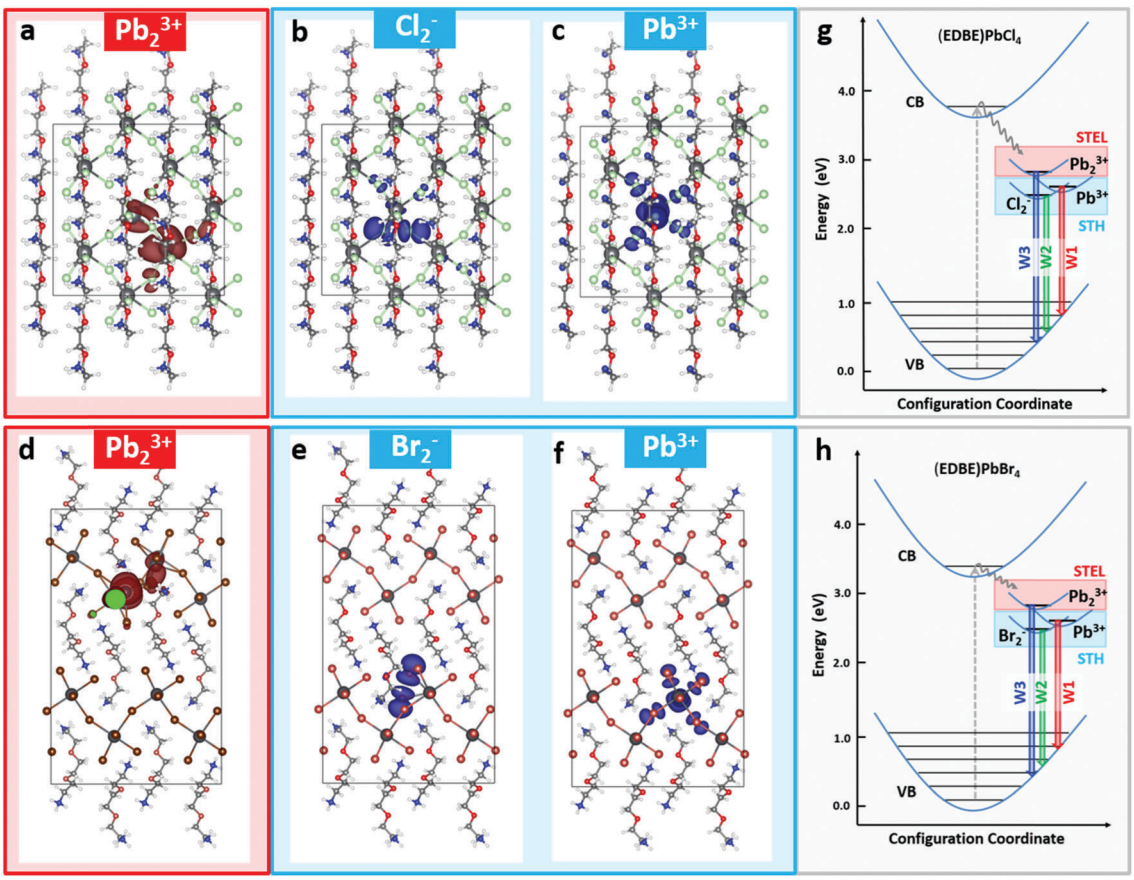

Fig. 5 Charge density mappings and exciton relaxation model. Charge density calculated for (EDBE)$PbCl_4$ (a, electrons, b and c holes) and (EDBE)$PbBr_4$ (d, electrons, e and f holes) upon perturbation of selected crystal lattice sites at the PBE/wSOC level. The applied perturbations involve shortening of the Pb–Pb (a and d), X–X (b and e) and Pb–X (c and f) distances, with the resulting charge localization showing the formation of self-trapped electrons (STEL) Pb_2^{3+} and self-trapped holes (STH) X_2^-, Pb^{3+} in the form of small polarons localized in the metal–halide framework. Schematic representation of the emissive process *via* polaron formation involved in the white-light generation of (g) (EDBE)$PbCl_4$ and (h) (EDBE)$PbBr_4$. Conversion of a Wannier–Mott exciton into a polaronic exciton (PE) proceeds *via* formation of self-trapped electrons (STEL) on Pb_2^{3+} sites, and self-trapped holes (STH) on Pb^{3+} and X_2^- (X = Cl, Br) states. The relative energies of these species were also determined (Fig. S11, ESI†). Radiative decay from each of these self-trapped states results in the three main emission bands observed in steady-state and time-resolved photoluminescence (*W1*, *W2*, and *W3*).

and broad photoluminescence.[48–51] In this case, electron-spin resonance (ESR) measurements have also identified the self-trapping centres to be Pb_2^{3+} for STEL, and Pb^{3+} and X_2^- (X = Cl, Br) for STH.[45,49,51–56] The latter, also known as V_k centers,[57,58] are commonly observed in alkali halides,[47] where hole trapping strengthens the interaction between halide pairs leading to the formation of dimer species X_2^- within the ionic crystal.[45]

We previously discussed how the organic cations in 2D EDBE perovskites are responsible for the formation of a layered structure, where charges are strongly confined in inter-layer potential wells and subject to strong electron–phonon interactions. Yet, optical transitions are mainly related to the inorganic layers originating from the lead halide precursors PbX_2, and the photoexcitation properties are very similar to those of lead halides PbX_2.[59] It is then reasonable to expect the occurrence of charge self-trapping effects in EDBE perovskites, similar to those in PbX_2. To prove this hypothesis, we computed the charge density maps for holes and electrons in (EDBE)$PbCl_4$ (Fig. 5a–c) and (EDBE)$PbBr_4$ (Fig. 5d–f) in which dimerization has been introduced as a perturbation in the crystal lattice. We first constructed the 2D perovskite supercell models and exerted local perturbations, where selective bond lengths of nearest neighbour atoms (Pb–Pb, Pb–X, and X–X) were shortened to induce the local structural deformations. The charge density distributions of the VBM and CBM were finally plotted based on the PBE/wSOC results.

Compared to the unperturbed systems, where charges are fully delocalized in the inorganic framework (Fig. S9 and S10, ESI†), the Pb–Pb dimerization causes selective localization of electron density close to the strained lattice point in both perovskites, which is consistent with the self-trapping of electrons at Pb_2^{3+} sites (Fig. 1a and d) previously observed in lead halides.[52–54] On the other hand, hole self-localization occurs with Cl–Cl and Br–Br pairing, driving the formation of V_k centres Cl_2^- and Br_2^- for the chloride and bromide perovskite, respectively (Fig. 5b and e). Hole density localization can also occur at Pb^{2+} sites leading to the formation of Pb^{3+} centres, coupled with the lattice deformation involving shortening of Pb–X bond lengths around the localization site (Fig. 5c and f). A similar behaviour was previously observed in AgCl, where hole localization at Ag^+ sites causes the tetragonal distortion of the surrounding lattice.[60] Overall, X_2^- and Pb^{3+} correspond to two distinct self-trapped holes. Interestingly, the results of the calculations in Fig. 5a–f show that similar polaronic species form in both EDBE perovskites, irrespective of the ⟨100⟩ or ⟨110⟩ orientations, which indicates that exciton localization occurs independently of the planarity of the octahedra coordination planes (Fig. 1).[31]

At this stage, by combining our experimental and computational results, we can propose the following model for the mechanism of white-light emission in (EDBE)PbX_4 (Fig. 5g and h). Upon resonant photoexcitation of the E-band, Wannier–Mott excitons are generated within the potential wells of the inorganic interlayers of 2D perovskites. Electrons and holes in the bound exciton pairs self-localize in the crystal lattice, converting these Wannier–Mott excitons into polaron–excitons with reduced average binding energy of the order of 100–150 meV (corresponding to the activation energy determined in Fig. S5, ESI†). This leads to the formation of self-trapped electron (STEL) Pb_2^{3+} and self-trapped hole (STH) Pb^{3+} and X_2^- states with relative energies $E^{STH}_{X_2^-} < E^{STH}_{Pb^{3+}} < E^{STEL}_{Pb_2^{3+}}$, which define the specific polaronic emissive states (Fig. S11, ESI†). It is likely that inter-band absorption at higher photon energies activates alternative non-radiative relaxation channels, preventing the formation of self-trapped polaron–excitons. Electron–hole annihilation associated to STEL contributes to light emission corresponding to the *W*3 band; similarly, the polaronic excitons deriving from the STH states recombine radiatively leading to the *W*1 and *W*2 photoluminescence bands.[61] Hole trapping appears to be more efficient than electron trapping at low temperature, increasing the weight of STH luminescence, consistent with previous calculations which predict smaller localization energy for holes compared to electrons in alkali halides.[62] Strong electron–phonon coupling involved in polaron formation explains the large Stokes shift observed experimentally, and further broadens the bandwidth of radiative transitions. Although the organic layer is not actively involved in polaron formation, charge confinement in the layered structure significantly increases the carrier effective masses,[63] strengthening electron–phonon coupling and fostering polaron formation even at room temperature. Thus, this model is not expected to be limited to EDBE-based perovskites, but shall apply to a wide family of materials with large electron–phonon coupling; this includes mono and two-dimensional perovskites, as well as 3D structures in which the lattice is distorted by photoexcitation or other physical and chemical means (*e.g.*, hydrostatic pressure, compositional and stoichiometric tuning).

Conclusion

We have conducted a combined, systematic spectroscopic and computational study of the white-light emission properties of layered organic–inorganic perovskites (EDBE)$PbCl_4$ and (EDBE)$PbBr_4$. The results allow us to formulate a comprehensive model of exciton relaxation dynamics leading to their unusually large Stokes shift and white broadband photoluminescence. We also provide both theoretical and experimental evidence for the formation of self-localized polarons and identify polaron–excitons Pb_2^{3+}, Pb^{3+}, and X_2^- (X = Cl, Br) localized within the inorganic lattice as the intra-gap emissive species.

Overall, these findings prompt wider consideration of the role of electron–phonon interactions and structural deformations on the optoelectronic properties of perovskites. Structural distortion of the soft lattice may be engineered to improve charge transport properties of highly luminescent 2D perovskites for light-emitting diodes and displays. This concept might be explored to tune the ratio of excitons and charge carriers in 3D perovskite materials, with potential relevance to transistors and solar cell devices.

Methods

Perovskite synthesis

2,2′-(Ethylenedioxy)bis(ethylamine) (98%), hydrochloric acid (HCl, 37% H_2O) hydrobromic acid (HBr, 48% in H_2O), lead(II)

chloride ($PbCl_2$, 99.999% trace metal basis), lead(II) bromide ($PbBr_2$, 99.999% trace metal basis) and dimethyl sulfoxide (DMSO, anhydrous 99,9%) were purchased from Sigma-Aldrich. Quartz cuvettes (four sides clear, 20 mm path length, wavelength range: 170–2700 nm) for optical measurements in N_2 inert atmosphere were purchased from Achema Pte Ltd, and quartz substrates from Crystran Ltd. (EDBE)Cl_2 was synthetized by reaction of 1 equivalent of HCl (37% in H_2O) with 2,2′-(ethylenedioxy)bis(ethylamine) for 2 h at 0 °C. (EDBE)Br_2 was synthetized by reaction of 3 equivalents of HCl (48% in H_2O) with 2,2′-(ethylenedioxy)bis(ethylamine) for 2 h at 0 °C. The resulting white hygroscopic salts were collected with a rotary evaporator, dried in a vacuum oven overnight at 60 °C and stored in a glove box (N_2 atmosphere). (EDBE)$PbCl_4$ was prepared by mixing (EDBE)Cl_2 and $PbCl_2$ (1 : 1 molar ratio), while (EDBE)Br_2 and PbBr2 (1 : 1 molar ratio) were mixed to prepare (EDBE)$PbBr_4$. In all cases, solutions with the desired concentration (0.1 M, 0.25 M and 0.5 M) were prepared in DMSO dissolving the powders at 100 °C for 1 h. The films were prepared by spinning the hot solution (100 °C) on cold substrates at 4000 rpm, for 60 s, and annealing for 15 minutes on a hotplate (100 °C). The perovskite deposition was performed in a glove-box under N_2 environment.

Structural and morphological characterization

X-ray diffraction characterization of perovskite thin films was performed using a BRUKER D8 ADVANCE with Bragg–Brentano geometry employing Cu Kα radiation (λ =1.54056 Å), step increment of 0.02° and 1 s of acquisition time. Raman spectra were obtained in a Renishaw Raman microscope configured with a charge coupled device array detector. A laser line (λ_{ex} = 532 nm) was used for excitation with power below 1 mW. Raman signals were collected by a Leica 1003 objective lens (NA = 50.85) and dispersed by 2400 line per mm gratings with frequency resolution of 0.8 cm^{-1}. The integration time was 20 s.

Optical characterization

Thin film samples were deposited on quartz substrates and mounted into a liquid nitrogen-cooled Linkam Stage (FTIR 600) that allows operating temperatures down to 77 K to be reached. Absorption spectra were recorded by an UV-VIS-NIR spectrophotometer (UV3600, Shimadzu) using a scanning resolution of 0.1 nm. Steady-state photoluminescence spectra were recorded by a Fluorolog-3, (HORIBA Jobin Yvon) spectrofluorometer with wavelength resolution 0.5 nm. Principal component fitting of absorption and emission lineshapes was performed using Voigt line profiles to account for the convolution of multiple broadening mechanisms. Time-resolved fluorescence was measured by a time-correlated single photon counting (TCSPC) technique with a resolution of 10 ps (PicoQuant PicoHarp 300). The second harmonic of a Titanium sapphire laser (Chameleon, Coherent Inc.) at 400 nm (100 fs, 80 MHz) was used as the excitation source. The kinetics of fluorescence from 438 to 579 nm were recorded. A deconvolution/fit procedure was applied in order to obtain the time components of fluorescence decay. A home built pump–probe setup is used for our transient absorption measurement. A commercial amplifier system, Quantronix Integra-C is used as the laser source at the repetition rate of 1 KHz and pulse width of 100 fs. Broadband white light with the highest cutoff photon energy at 3.54 eV (350 nm) is generated in a 3 mm thick calcium fluoride crystal *via* white light continuum generation. To prevent laser induced damage, the crystal is constantly spun during the measurements. A commercial spectrometer, Jobin Yvon CP140-104, equipped with a silicon photodiode array is used to record the transient absorption spectra (Entwicklungsbüro Stresing). To remove higher diffraction order artefacts in the measurement, a shortwave pass filter is used to cut off the low energy end of the white light spectrum at 1.77 eV (700 nm). A pump wavelength of 266 nm is generated by first generating 400 nm using a type I BBO crystal and subsequently followed by third harmonic generation using another BBO crystal cut for sum frequency generation with the generated 400 and residue 800 nm. Pump wavelengths of 330 and 370 nm were generated by doubling the output of a commercial optical parametric amplifier, Quantronix Palitra running at 660 nm and 740 nm respectively with a 1 mm thick BBO crystal cut at 29.2°. To reduce white light stability artefacts in the measured transient absorption spectra, selected spectra at different time delays were obtained for 3000 measurement cycles while the kinetic spectra were obtained for 900 measurement cycles for a reasonable measurement time.

Computational methods

Structural optimization, band structure, and charge density calculations were performed using the Vienna *ab initio* Simulation Package (VASP).[64,65] The projector augmented-wave (PAW) method was used with a PBE exchange–correlation functional to describe the electron–ion interactions with electronic orbitals of H (1s); O, N and C (2s, 2p); Cl (3s, 3p); Br (4s, 4p) and Pb (5d, 6s, 6p). The plane-wave basis set cutoffs of the wave functions were set to 500 eV; 4 × 4 × 4 and 4 × 2 × 4 Monkhorst–Pack grids were chosen for sampling the Brillouin zone of (EDBE)$PbCl_4$ and (EDBE)$PbBr_4$, respectively. The experimental crystal structures for both monoclinic crystals reported by Dohner *et al.*[22] were used as an initial guess, and both lattice and atomic coordinates were relaxed using the method of Broyden–Fletcher–Goldfarb–Shanno (BFGS) until the residual atomic forces were less than 0.01 eV $Å^{-1}$. The hole and electron densities under four possible perturbations (corresponding to shortenings of specific bond lengths) were plotted to simulate the formation of self-trapped charges in the periodically repeated 2 × 2 × 1 supercells. The molecular graphics viewer VESTA was used to plot the molecular structures and charge densities.

Acknowledgements

We thank Ting Ting for help with Raman measurements. Research at NTU was supported by the Ministry of Education (ref. No. MOE2013-T2-1-044 and MOE2011-T3-1-005) and the National Research Foundation (ref. No. NRF-CRP14-2014-03) of Singapore. JY and JLB acknowledge support from the King Abdullah University of Science and Technology and thank the

IT Research Computing Team and Supercomputing Laboratory at KAUST for computational and storage resources.

References

1 P. Gao, M. Gratzel and M. K. Nazeeruddin, *Energy Environ. Sci.*, 2014, **7**, 2448–2463.
2 S. Yakunin, M. Sytnyk, D. Kriegner, S. Shrestha, M. Richter, G. J. Matt, H. Azimi, C. J. Brabec, J. Stangl, M. V. Kovalenko and W. Heiss, *Nat. Photonics*, 2015, **9**, 444–449.
3 S. D. Stranks and H. J. Snaith, *Nat. Nanotechnol.*, 2015, **10**, 391–402.
4 H. Cho, S.-H. Jeong, M.-H. Park, Y.-H. Kim, C. Wolf, C.-L. Lee, J. H. Heo, A. Sadhanala, N. Myoung, S. Yoo, S. H. Im, R. H. Friend and T.-W. Lee, *Science*, 2015, **350**, 1222–1225.
5 Z.-K. Tan, R. S. Moghaddam, M. L. Lai, P. Docampo, R. Higler, F. Deschler, M. Price, A. Sadhanala, L. M. Pazos, D. Credgington, F. Hanusch, T. Bein, H. J. Snaith and R. H. Friend, *Nat. Nanotechnol.*, 2014, **9**, 687–692.
6 X. Y. Chin, D. Cortecchia, J. Yin, A. Bruno and C. Soci, *Nat. Commun.*, 2015, **6**, 7383.
7 G. Xing, N. Mathews, S. S. Lim, N. Yantara, X. Liu, D. Sabba, M. Grätzel, S. Mhaisalkar and T. C. Sum, *Nat. Mater.*, 2014, **13**, 476–480.
8 V. D'Innocenzo, A. R. Srimath Kandada, M. De Bastiani, M. Gandini and A. Petrozza, *J. Am. Chem. Soc.*, 2014, **136**, 17730–17733.
9 D. B. Mitzi, *Progress in Inorganic Chemistry*, John Wiley & Sons, Inc., 2007, ch1, pp. 1–121, DOI: 10.1002/9780470166499.
10 D. B. Mitzi, *Functional Hybrid Materials*, Wiley-VCH Verlag GmbH & Co. KGaA, 2005, pp. 347–386, DOI: 10.1002/3527602372.ch10.
11 T. Ishihara, *Optical Properties of Low – Dimensional Materials*, 1996, pp. 288–339, DOI: 10.1142/9789814261388_0006.
12 E. A. Muljarov, S. G. Tikhodeev, N. A. Gippius and T. Ishihara, *Phys. Rev. B: Condens. Matter Mater. Phys.*, 1995, **51**, 14370–14378.
13 P. P. Boix, S. Agarwala, T. M. Koh, N. Mathews and S. G. Mhaisalkar, *J. Phys. Chem. Lett.*, 2015, **6**, 898–907.
14 M. Yuan, L. N. Quan, R. Comin, G. Walters, R. Sabatini, O. Voznyy, S. Hoogland, Y. Zhao, E. M. Beauregard, P. Kanjanaboos, Z. Lu, D. H. Kim and E. H. Sargent, *Nat. Nanotechnol.*, 2016, **11**, 872–877.
15 Q. Wang and D. Ma, *Chem. Soc. Rev.*, 2010, **39**, 2387–2398.
16 W. Ki, J. Li, G. Eda and M. Chhowalla, *J. Mater. Chem.*, 2010, **20**, 10676–10679.
17 W. Ki and J. Li, *J. Am. Chem. Soc.*, 2008, **130**, 8114–8115.
18 M. Roushan, X. Zhang and J. Li, *Angew. Chem., Int. Ed.*, 2012, **51**, 436–439.
19 M. J. Bowers, J. R. McBride and S. J. Rosenthal, *J. Am. Chem. Soc.*, 2005, **127**, 15378–15379.
20 Y. Y. Li, C. K. Lin, G. L. Zheng, Z. Y. Cheng, H. You, W. D. Wang and J. Lin, *Chem. Mater.*, 2006, **18**, 3463–3469.
21 E. R. Dohner, E. T. Hoke and H. I. Karunadasa, *J. Am. Chem. Soc.*, 2014, **136**, 1718–1721.
22 E. R. Dohner, A. Jaffe, L. R. Bradshaw and H. I. Karunadasa, *J. Am. Chem. Soc.*, 2014, **136**, 13154–13157.
23 A. Yangui, D. Garrot, J. S. Lauret, A. Lusson, G. Bouchez, E. Deleporte, S. Pillet, E. E. Bendeif, M. Castro, S. Triki, Y. Abid and K. Boukheddaden, *J. Phys. Chem. C*, 2015, **119**, 23638–23647.
24 T. Hu, M. D. Smith, E. R. Dohner, M.-J. Sher, X. Wu, M. T. Trinh, A. Fisher, J. Corbett, X. Y. Zhu, H. I. Karunadasa and A. M. Lindenberg, *J. Phys. Chem. Lett.*, 2016, **7**, 2258–2263.
25 T. Kenichiro, T. Takayuki, K. Takashi, U. Kenichi, E. Kazuhiro, U. Tsutomu, A. Keisuke, U. Kazuhito and M. Noboru, *Jpn. J. Appl. Phys.*, 2005, **44**, 5923.
26 D. B. Straus, S. Hurtado Parra, N. Iotov, J. Gebhardt, A. M. Rappe, J. E. Subotnik, J. M. Kikkawa and C. R. Kagan, *J. Am. Chem. Soc.*, 2016, **138**, 13798–13801.
27 R. G. Niemann, A. G. Kontos, D. Palles, E. I. Kamitsos, A. Kaltzoglou, F. Brivio, P. Falaras and P. J. Cameron, *J. Phys. Chem. C*, 2016, **120**, 2509–2519.
28 R. A. Abreu, *Phys. Lett. A*, 1984, **100**, 375–378.
29 A. M. A. Leguy, P. Azarhoosh, M. I. Alonso, M. Campoy-Quiles, O. J. Weber, J. Yao, D. Bryant, M. T. Weller, J. Nelson, A. Walsh, M. van Schilfgaarde and P. R. F. Barnes, *Nanoscale*, 2016, **8**, 6317–6327.
30 Z. Cheng and J. Lin, *CrystEngComm*, 2010, **12**, 2646–2662.
31 D. Cortecchia, S. Neutzner, A. R. Srimath Kandada, E. Mosconi, D. Meggiolaro, F. De Angelis, C. Soci and A. Petrozza, *J. Am. Chem. Soc.*, 2017, **139**, 39–42.
32 Y. Fang, L. Wang, Q. Sun, T. Lu, Z. Deng, Z. Ma, Y. Jiang, H. Jia, W. Wang, J. Zhou and H. Chen, *Sci. Rep.*, 2015, **5**, 12718.
33 J. L. Bredas and G. B. Street, *Acc. Chem. Res.*, 1985, **18**, 309–315.
34 A. J. Heeger, *J. Phys. Chem. B*, 2001, **105**, 8475–8491.
35 X. Y. Zhu and V. Podzorov, *J. Phys. Chem. Lett.*, 2015, **6**, 4758–4761.
36 K. Gauthron, J. S. Lauret, L. Doyennette, G. Lanty, A. Al Choueiry, S. J. Zhang, A. Brehier, L. Largeau, O. Mauguin, J. Bloch and E. Deleporte, *Opt. Express*, 2010, **18**, 5912–5919.
37 A. M. Soufiani, F. Huang, P. Reece, R. Sheng, A. Ho-Baillie and M. A. Green, *Appl. Phys. Lett.*, 2015, **107**, 231902.
38 F. Maddalena, P. P. Boix, C. Xin Yu, N. Mathews, C. Soci and S. Mhaisalkar, in *Organic-Inorganic Halide Perovskite Photovoltaics: From Fundamentals to Device Architectures*, ed. N.-G. Park, M. Grätzel and T. Miyasaka, Springer International Publishing, Cham, 2016, pp. 201–222, DOI: 10.1007/978-3-319-35114-8_8.
39 C. Wehrenfennig, M. Liu, H. J. Snaith, M. B. Johnston and L. M. Herz, *J. Phys. Chem. Lett.*, 2014, **5**, 1300–1306.
40 W. Nie, J.-C. Blancon, A. J. Neukirch, K. Appavoo, H. Tsai, M. Chhowalla, M. A. Alam, M. Y. Sfeir, C. Katan, J. Even, S. Tretiak, J. J. Crochet, G. Gupta and A. D. Mohite, *Nat. Commun.*, 2016, **7**, 11574.
41 A. J. Neukirch, W. Nie, J.-C. Blancon, K. Appavoo, H. Tsai, M. Y. Sfeir, C. Katan, L. Pedesseau, J. Even, J. J. Crochet, G. Gupta, A. D. Mohite and S. Tretiak, *Nano Lett.*, 2016, **16**, 3809–3816.
42 G. Borstel, R. I. Eglitis, E. A. Kotomin and E. Heifets, *Phys. Status Solidi B*, 2003, **236**, 253–264.
43 V. S. Vikhnin, R. I. Eglitis, S. E. Kapphan, G. Borstel and E. A. Kotomin, *Phys. Rev. B: Condens. Matter Mater. Phys.*, 2002, **65**, 104304.

44 *Collected Papers of L.D. Landau*, ed. D. T. Haar, Pergamon, 1965, pp. 67–68, DOI: 10.1016/B978-0-08-010586-4.50015-8.
45 R. T. Williams and K. S. Song, *J. Phys. Chem. Solids*, 1990, **51**, 679–716.
46 N. F. Mott and A. M. Stoneham, *J. Phys. C: Solid State Phys.*, 1977, **10**, 3391.
47 A. N. Jette, T. L. Gilbert and T. P. Das, *Phys. Rev.*, 1969, **184**, 884–894.
48 V. Babin, A. Krasnikov, M. Nikl, A. Stolovits and S. Zazubovich, *Phys. Status Solidi B*, 2002, **229**, 1295–1304.
49 M. Iwanaga and T. Hayashi, *J. Lumin.*, 2003, **102–103**, 663–668.
50 R. Kink, T. Avarmaa, V. Kisand, A. Lõhmus, I. Kink and I. Martinson, *J. Phys.: Condens. Matter*, 1998, **10**, 693.
51 M. Kitaura and H. Nakagawa, *J. Lumin.*, 1997, **72–74**, 883–884.
52 S. V. Nistor and D. Schoemaker, *Phys. Status Solidi B*, 1995, **190**, 339–346.
53 M. Iwanaga, J. Azuma, M. Shirai, K. Tanaka and T. Hayashi, *Phys. Rev. B: Condens. Matter Mater. Phys.*, 2002, **65**, 214306.
54 S. V. Nistor, E. Goovaerts and D. Schoemaker, *Phys. Rev. B: Condens. Matter Mater. Phys.*, 1993, **48**, 9575–9580.
55 H. Toyoharu, F. Toshiaki and K. Yukio, *Jpn. J. Appl. Phys.*, 1993, **32**, 4674.
56 M. Iwanaga, M. Shirai, K. Tanaka and T. Hayashi, *Phys. Rev. B: Condens. Matter Mater. Phys.*, 2002, **66**, 064304.
57 W. Känzig, *Phys. Rev.*, 1955, **99**, 1890–1891.
58 T. G. Castner and W. Känzig, *J. Phys. Chem. Solids*, 1957, **3**, 178–195.
59 G. Liidja and V. Plekhanov, *J. Lumin.*, 1973, **6**, 71–76.
60 I. Pelant and J. Valenta, *Luminescence Spectroscopy of Semiconductors*, OUP Oxford, 2012.
61 P. A. Rodnyi, *Physical processes in inorganic scintillators*, CRC press, 1997.
62 J. H. Crawford and L. M. Slifkin, *Point Defects in Solids: General and Ionic Crystals*, Springer US, 2013.
63 D. Cortecchia, H. A. Dewi, J. Yin, A. Bruno, S. Chen, T. Baikie, P. P. Boix, M. Grätzel, S. Mhaisalkar, C. Soci and N. Mathews, *Inorg. Chem.*, 2016, **55**, 1044–1052.
64 G. Kresse and J. Furthmüller, *Comput. Mater. Sci.*, 1996, **6**, 15–50.
65 G. Kresse and D. Joubert, *Phys. Rev. B: Condens. Matter Mater. Phys.*, 1999, **59**, 1758–1775.